Astronomy & Astrophysics

The GAPS Programme with HARPS-N at TNG[*],[**],[***]

VIII. Observations of the Rossiter-McLaughlin effect and characterisation of the transiting planetary systems HAT-P-36 and WASP-11/HAT-P-10

L. Mancini[1,2], M. Esposito[3,4], E. Covino[5], G. Raia[5], J. Southworth[6], J. Tregloan-Reed[7], K. Biazzo[8], A. S. Bonomo[2], S. Desidera[9], A. F. Lanza[8], G. Maciejewski[10], E. Poretti[11], A. Sozzetti[2], F. Borsa[11], I. Bruni[12], S. Ciceri[1], R. Claudi[9], R. Cosentino[13], R. Gratton[9], A. F. Martinez Fiorenzano[13], G. Lodato[14], V. Lorenzi[13], F. Marzari[9,13], S. Murabito[3,4], L. Affer[15], A. Bignamini[16], L. R. Bedin[9], C. Boccato[9], M. Damasso[2], Th. Henning[1], A. Maggio[15], G. Micela[15], E. Molinari[13,17], I. Pagano[8], G. Piotto[9,18], M. Rainer[11], G. Scandariato[8], R. Smareglia[16], and R. Zanmar Sanchez[8]

[1] Max Planck Institute for Astronomy, Königstuhl 17, 69117 Heidelberg, Germany
e-mail: mancini@mpia.de
[2] INAF – Osservatorio Astrofisico di Torino, via Osservatorio 20, 10025 Pino Torinese, Italy
[3] Instituto de Astrofísica de Canarias, C/ vía Láctea s/n, 38205 La Laguna, Tenerife, Spain
[4] Dep. de Astrofísica, Universidad de La Laguna, Avda. Astrofísico F. Sánchez s/n, 38206 La Laguna, Tenerife, Spain
[5] INAF – Osservatorio Astronomico di Capodimonte, via Moiariello 16, 80131 Naples, Italy
[6] Astrophysics Group, Keele University, Keele ST5 5BG, UK
[7] NASA Ames Research Center, Moffett Field, CA 94035, USA
[8] INAF – Osservatorio Astrofisico di Catania, via S. Sofia 78, 95123 Catania, Italy
[9] INAF – Osservatorio Astronomico di Padova, Vicolo dell'Osservatorio 5, 35122 Padova, Italy
[10] Centre for Astronomy, Nicolaus Copernicus University, Grudziadzka 5, 87-100 Torun, Poland
[11] INAF – Osservatorio Astronomico di Brera, via E. Bianchi 46, 23807 Merate (Lecco), Italy
[12] INAF – Osservatorio Astronomico di Bologna, via Ranzani 1, 40127 Bologna, Italy
[13] Fundación Galileo Galilei – INAF, Rambla José Ana Fernandez Pérez, 738712 Breña Baja, Tenerife, Spain
[14] Dipartimento di Fisica, Università di Milano, via Celoria 16, 20133 Milano, Italy
[15] INAF – Osservatorio Astronomico di Palermo, Piazza del Parlamento, 90134 Palermo, Italy
[16] INAF – Osservatorio Astronomico di Trieste, via Tiepolo 11, 34143 Trieste, Italy
[17] INAF – IASF Milano, via Bassini 15, 20133 Milano, Italy
[18] Dip. di Fisica e Astronomia Galileo Galilei, Università di Padova, Vicolo dell'Osservatorio 2, 35122 Padova, Italy

ABSTRACT

Context. Orbital obliquity is thought to be a fundamental parameter in tracing the physical mechanisms that cause the migration of giant planets from the snow line down to roughly 10^{-2} au from their host stars. We are carrying out a large programme to estimate the spin-orbit alignment of a sample of transiting planetary systems to study what the possible configurations of orbital obliquity are and whether they correlate with other stellar or planetary properties.

Aims. We determine the true and the projected obliquity of HAT-P-36 and WASP-11/HAT-P-10 systems, respectively, which are both composed of a relatively cool star (with effective temperature $T_{\rm eff} < 6100$ K) and a hot-Jupiter planet.

Methods. Thanks to the high-resolution spectrograph HARPS-N, we observed the Rossiter-McLaughlin effect for both systems by acquiring precise ($3-8$ m s^{-1}) radial-velocity measurements during planetary transit events. We also present photometric observations comprising six light curves that cover five transit events, which were obtained using three medium-class telescopes. One transit of WASP-11/HAT-P-10 was followed simultaneously from two observatories. The three transit light curves of HAT-P-36 b show anomalies that are attributable to starspot complexes on the surface of the parent star, in agreement with the analysis of its spectra that indicates moderate activity (log $R'_{\rm HK} = -4.65$ dex). By analysing the complete HATNet data set of HAT-P-36, we estimated the stellar rotation period by detecting a periodic photometric modulation in the light curve caused by star spots, obtaining $P_{\rm rot} = 15.3 \pm 0.4$ days, which implies that the inclination of the stellar rotational axis with respect to the line of sight is $i_\star = 65° \pm 34°$.

Results. We used the new spectroscopic and photometric data to revise the main physical parameters and measure the sky-projected misalignment angle of the two systems. We found $\lambda = -14° \pm 18°$ for HAT-P-36 and $\lambda = 7° \pm 5°$ for WASP-11/HAT-P-10, indicating in both cases a good spin-orbit alignment. In the case of HAT-P-36, we were also able to estimate an upper limit of its real obliquity, which turned out to be $\psi < 63$ degrees.

Key words. planetary systems – stars: fundamental parameters – techniques: photometric – techniques: radial velocities – stars: individual: HAT-P-36 – stars: individual: WASP-11/HAT-P-10

---

[*] Based on observations made with (i) the Italian 3.58 m Telescopio Nazionale *Galileo* at the Observatory of Roque de los Muchachos; (ii) the *Cassini* 1.52 m telescope at the Astronomical Observatory of Bologna; (iii) the Zeiss 1.23 m telescope at the Observatory of Calar Alto, and the IAC 80 cm telescope at the Teide Observatory.

[**] Table 1 and Appendix A are available in electronic form at http://www.aanda.org

[***] Data of the light curves are only available at the CDS via anonymous ftp to cdsarc.u-strasbg.fr (130.79.128.5) or via http://cdsarc.u-strasbg.fr/viz-bin/qcat?J/A+A/579/A136

1. Introduction

Since its discovery (Mayor & Queloz 1995), hot Jupiters have challenged the community of theoretical astrophysicists to explain their existence. They are a population of gaseous giant extrasolar planets, similar to Jupiter, but revolving very close to their parent stars (between ~0.01 and 0.05 au), which causes them to have orbital periods of a few days and high equilibrium temperatures (between ~400 and 2750 K)[1]. According to the generally accepted theory of planet formation (we refer the reader to the recent review of Mordasini et al. 2015), hot Jupiters are thought to form far from their parent stars, beyond the so-called snow line, and then migrate inwards to their current positions at a later time. However, the astrophysical mechanism that regulates this migration process, such as the one that causes planets to move on misaligned orbits, is still a matter of debate.

Spin-orbit obliquity, ψ, which is the angle between a planet's orbital axis and its host star's spin, could be the primary tool for understanding the physics behind the migration process of giant planets (e.g., Dawson 2014, and references therein). A broad distribution of ψ is expected for giant planets, whose orbits are originally large (beyond the snow line) and (being perturbed by other bodies) highly eccentric, and then become smaller and circularise by the planet's tidal dissipation during close periastron passages. Instead, a much smoother migration, like the one through a proto-planetary disc, should preserve a good spin-orbit alignment and, assuming that the axis of the proto-planetary disk remains constant with time, imply a final hot-Jupiter population with $\psi \simeq 0$.

The experimental measurement of ψ for a large sample of hot Jupiters is mandatory to guide our comprehension of such planetary evolution processes in the meanders of theoretical speculations. Unfortunately, this quantity is very difficult to determine, and only a few measurements exist (e.g., Brothwell et al. 2014; Lendl et al. 2014; Lund et al. 2014). However, its sky projection, λ, is a quantity that is commonly measured for stars hosting transiting exoplanets through the observation of the Rossiter-McLaughlin (RM) effect with high-precision radial-velocity (RV) instruments. Such measurements have revealed a wide range of obliquities in both early- and late-type stars (e.g., Triaud et al. 2010; Albrecht et al. 2012b), including planets revolving perpendicular (e.g., Albrecht et al. 2012a) or retrograde (e.g., Anderson et al. 2010; Hébrard et al. 2011; Esposito et al. 2014) to the direction of the rotation of their parent stars. The results collected so far are not enough to provide robust statistics, and more investigations are needed to infer a comprehensive picture for identifying what the most plausible hot-Jupiter migration channels are.

Within the framework of Global Architecture of Planetary Systems (GAPS), a manifold long-term observational programme that uses the high-resolution spectrograph HARPS-N at the 3.58 m TNG telescope for several semesters (Desidera et al. 2013, 2014; Damasso et al. 2015), we are carrying out a subprogramme aimed at studying the spin-orbit alignment of a large sample of known transiting extrasolar planet (TEP) systems (Covino et al. 2013). This subprogramme is supported by photometric follow-up observations of planetary-transit events of the targets in the sample list by using an array of medium-class telescopes. Monitoring new transits is useful for getting additional information, as stellar activity, and for constraining the whole set of physical parameters of the TEP systems

better. When possible, photometric observations are simultaneously performed with the measurement of the RM effect, benefiting from the two-telescope observational strategy (Ciceri et al. 2013).

Here, we present the results for two TEP systems: HAT-P-36 and WASP-11/HAT-P-10.

The paper is organized as follows. In Sect. 1.1 we briefly describe the two systems, subjects of this research study. The observations and reduction procedures are treated in Sect. 2, while Sect. 3 is dedicated to the analysis of the photometric data and the refining of the orbital ephemerides; anomalies detected in the HAT-P-36 light curves are also discussed. In Sect. 4 the HARPS-N time-series data are used to determine the stellar atmospheric properties and measure the spin-orbit relative orientation of both the systems. Section 5 is devoted to the revision of the main physical parameters of the two planetary systems, based on the data previously presented. The results of this work are finally discussed and summarised in Sect. 6.

1.1. Case history

HAT-P-36, discovered by the HAT-Net survey (Bakos et al. 2012), is composed of a $V = 12.5$ mag, G5 V star (this work), similar to our Sun, and a hot Jupiter (mass ~1.8 $M_{\rm Jup}$ and radius ~1.3 $R_{\rm Jup}$), which revolves around its parent star in nearly 1.3 days. The only follow-up study of this system has provided a refinement of the transit ephemeris based on the photometric observation of two planetary transits performed with a 0.6 m telescope (Maciejewski et al. 2013).

The discovery of the WASP-11/HAT-P-10 TEP system was almost concurrently announced by the WASP (West et al. 2009) and HAT-Net (Bakos et al. 2009) teams. It is composed of a $V = 11.9$ mag, K3 V star (Ehrenreich & Désert 2011) (mass ~0.8 $M_\odot$ and radius ~0.8 $R_\odot$) and a Jovian planet (mass ~0.5 $M_{\rm Jup}$ and radius ~1 $R_{\rm Jup}$), moving on a 3.7 day circular orbit. Four additional transit observations of this target were obtained by Sada et al. (2012) in z' and J bands with a 0.5 m and a 2.1 m telescope, respectively, which were used to refine the transit ephemeris and photometric parameters. In a more recent study (Wang et al. 2014), an additional four new light curves, which were obtained with a 1 m telescope, were presented and most of the physical parameters were revised, confirming the results of the two discovery papers.
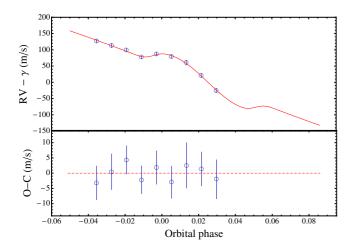
2. Observation and data reduction

In this section we present new spectroscopic and photometric follow-up observations of HAT-P-36 and WASP-11/HAT-P-10. For both these planetary systems, the RM effect was measured for the first time, and three complete transit light curves were acquired.
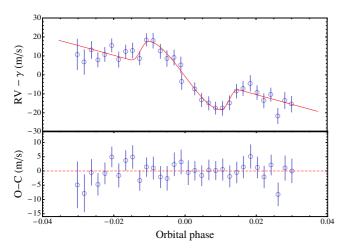
2.1. HARPS-N spectroscopic observations

Spectroscopic observations of the two targets were performed using the HARPS-N (High Accuracy Radial velocity Planet Searcher-North; Cosentino et al. 2012) spectrograph at the 3.58 m TNG, in the framework of the above-mentioned GAPS programme.

A sequence of spectra of HAT-P-36 was acquired on the night 2013 February 21 during a transit event of its planet, with an exposure time of 900 s. Unfortunately, because of high humidity, the observations were stopped before the transit was over

---

[1] Data taken from TEPcat (Transiting Extrasolar Planet Catalogue), available at www.astro.keele.ac.uk/jkt/tepcat/ (Southworth 2011).

Fig. 1. Phase-folded RV data of a partial transit of HAT-P-36 b observed with HARPS-N. Superimposed is the best-fitting RV-curve model. The corresponding residuals are plotted in the lower panel. Phase 0 corresponds to the time of the planet passing the periastron.

Fig. 2. Phase-folded RV data of a complete transit of WASP-11 b observed with HARPS-N. Superimposed is the best-fitting RV-curve model. The corresponding residuals are plotted in the *lower panel*.

and thus only nine measurements were obtained that cover a bit more than the first half of the transit.

A complete spectroscopic transit of WASP-11/HAT-P-10 b was recorded on 2014 October 2. A sequence of 32 spectra was obtained using an exposure time of 600 s.

The spectra were reduced using the latest version of the HARPS-N instrument Data Reduction Software pipeline. The pipeline also provides rebinned 1D spectra that we used for stellar characterisation (see summary Tables 8 and 9), in particular, to estimate the stellar effective temperature, $T_{\rm eff}$, and metal abundance [Fe/H] (see Sect. 4.1). Radial velocities were measured by applying the weighted cross-correlation function (CCF) method (Baranne et al. 1996; Pepe et al. 2002) and using a G2 and a K5 mask for HAT-P-36 and WASP-11/HAT-P-10, respectively. They are reported in Table 1 and plotted in Figs. 1 and 2, in which we can immediately note that the RM effect was successfully observed. It indicates low orbital obliquity for both systems.

2.2. Photometric follow-up observations of HAT-P-36

One transit of HAT-P-36 b was observed on 2013 April through a Gunn-*r* filter with the Bologna Faint Object Spectrograph

& Camera (BFOSC) imager mounted on the 1.52 m *Cassini* Telescope at the Astronomical Observatory of Bologna in Loiano, Italy. The CCD was used unbinned, giving a plate scale of 0.58 arcsec pixel^{-1}, for a total FOV of 13 arcmin × 12.6 arcmin. Two successive transits were observed on 2014 April by using the Zeiss 1.23 m telescope at the German-Spanish Astronomical Centre at Calar Alto, Spain. This telescope is equipped with the DLR-MKIII camera, which has 4000 × 4000 pixels, a plate scale of 0.32 arcsec pixel^{-1}, and a FOV of 21.5 arcmin × 21.5 arcmin. The observations were performed remotely, a Cousins-*I* filter was adopted, and the CCD was used unbinned, too. Details of the observations are reported in Table 2. As in previous uses of the two telescopes (e.g, Mancini et al. 2013a), the defocussing technique was adopted in all the observations to improve the quality of the photometric data remarkably. Telescopes were also autoguided.

The data were reduced with a modified version of the DEFOT pipeline, written in IDL[2], which is exhaustively described in Southworth et al. (2014). In brief, we created master calibration frames by median-combining individual calibration images and used them to correct the scientific images. A reference image was selected in each data set and used to correct pointing variations. The target and a suitable set of non-variable comparison stars were identified in the images, and three rings were placed interactively around them; the aperture radii were chosen based on the lowest scatter achieved when compared with a fitted model. Differential photometry was finally measured using the APER routine[3]. Light curves were created with a second-order polynomial fitted to the out-of-transit data. The comparison star weights and polynomial coefficients were fitted simultaneously in order to minimise the scatter outside transit. Final light curves are plotted in Fig. 3 together with one, obtained by phasing/binning the four light curves reported in the discovery paper (Bakos et al. 2012), shown here just for comparison.
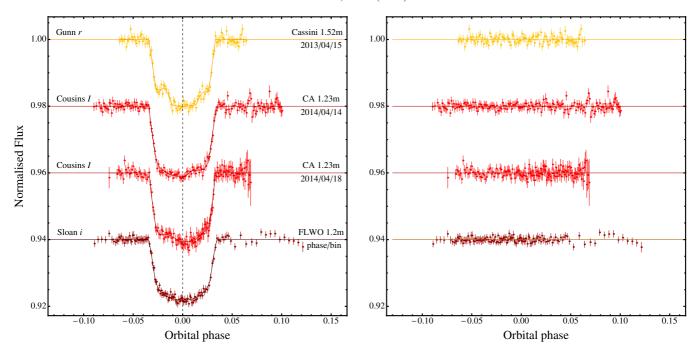
Very interestingly, the light curves present anomalies attributable to the passage of the planetary shadow over starspots or starspot complexes on the photosphere of the host star, which show up in a weak and strong fashion. In particular, the transit observed with the *Cassini* telescope was also observed by the Toruń 0.6 m telescope (Maciejewski et al. 2013), which confirms the presence of anomalies in the light curves.

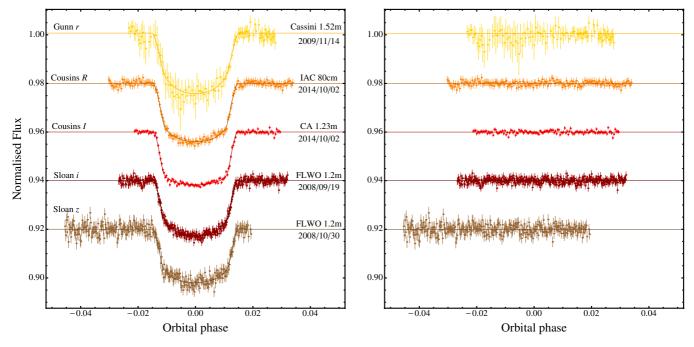### 2.3. Photometric follow-up observations of WASP-11/HAT-P-10

A transit observation of WASP-11/HAT-P-10 b was performed on 2009 November with the *Cassini* 1.52 m telescope through a Gunn-*r* filter. Unfortunately, the weather conditions were not optimal and the data were badly affected by the poor transparency of the sky. The same transit monitored by HARPS-N (2014 October 2) was also observed by the Zeiss 1.23 m telescope through a Cousins-*I* filter and a more adequate seeing (~0.7″). The characteristics of the two telescopes and observation modus operandi have already been described in the previous section. Moreover, the identical transit was observed with a third telescope, the IAC 80 cm telescope, located at the Teide Observatory on the island of Tenerife (Spain). The optical channel of this telescope is equipped with CAMELOT, a 2048 × 2048

---

[2] The acronym IDL stands for Interactive Data Language and is a trademark of ITT Visual Information Solutions.

[3] APER is part of the ASTROLIB subroutine library distributed by NASA.

Fig. 3. Light curves of HAT-P-36 b transits compared with the best PRISM+GEMC fits. The dates, the telescopes, and the filters used for each transit event are indicated. Residuals from the fits are displayed in the *right panel*. Starting from the top, the first three light curves (this work) present anomalies that we interpret as occultations of starspot complexes by the planet. The third light curve is related to the transit event successive to that of the second one. The last light curve was extracted from Bakos et al. (2012) and reported here for comparison. Here Phase 0 corresponds to the mid-time of the transit.

Fig. 4. Light curves of WASP-11/HAT-P-10 b transits compared with the best JKTEBOP fits. The dates, the telescopes, and the filters used for each transit event are indicated. Residuals from the fits are displayed in the *right panel*. Starting from the top, the first three light curves are from this work, whereas the last two are from Bakos et al. (2009). The second and third light curves are related to the same transit event.

CCD detector with a plate scale of 0.304 arcsec pixel^{-1}, providing an astronomical FOV of 10.4 arcmin × 10.4 arcmin. Details of these three WASP-11/HAT-P-10 b transit observations are reported in Table 2. The data sets were reduced in the same way as for the HAT-P-36 case (Sect. 2.2) and the corresponding light curves are shown in Fig. 4, together with two others taken from Bakos et al. (2009). The simultaneous transit observation is highlighted in Fig. 5, and it allowed an extremely

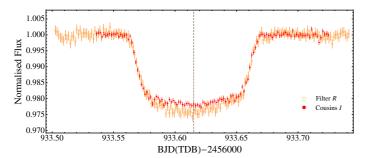precise measurements of the mid-point transit time, i.e., $T_0 = 2\,456\,933.615069 \pm 0.000075$ BJD(TDB).

3. Light-curve analysis

The three HAT-P-36 light curves show possible starspot crossing events, which must be analysed using a self-consistent and

Table 2. Details of the transit observations presented in this work.

Telescope	Date of first obs	Start time (UT)	End time (UT)	N_{obs}	T_{exp} (s)	T_{obs} (s)	Filter	Airmass	Moon illum.	Aperture radii (px)	Scatter (mmag)
HAT-P-36:											
Cassini	2013 04 14	19:58	00:39	112	120	144	Gunn r	$1.05 \rightarrow 1.000 \rightarrow 1.17$	12%	16,45,65	1.12
CA 1.23 m	2014 04 14	19:50	02:08	176	80-120	92-132	Cousins I	$1.28 \rightarrow 1.009 \rightarrow 1.20$	98%	22,50,75	1.10
CA 1.23 m	2014 04 18	19:54	00:26	146	80-130	92-142	Cousins I	$1.22 \rightarrow 1.009 \rightarrow 1.06$	92%	22,50,75	1.30
WASP-11/HAT-P-10:											
Cassini	2009 11 14	23:02	03:36	101	90-150	114-174	Gunn r	$1.06 \rightarrow 1.02 \rightarrow 2.00$	9%	17,25,45	2.24
CA 1.23 m	2014 10 02	00:51	05:23	125	120	132	Cousins I	$1.12 \rightarrow 1.04 \rightarrow 1.21$	52%	23,33,60	0.65
IAC 80 cm	2014 10 01	23:56	05:39	179	90	115	Cousins R	$1.008 \rightarrow 1.000 \rightarrow 2.49$	52%	28,60,90	0.92

Notes. N_{obs} is the number of observations, T_{exp} is the exposure time, T_{obs} is the observational cadence, and "Moon illum." is the geocentric fractional illumination of the Moon at midnight (UT). The aperture sizes are the radii of the software apertures for the star, inner sky and outer sky, respectively. Scatter is the rms scatter of the data versus a fitted model.

Fig. 5. Light curve of a transit event of WASP-11/HAT-P-10 b observed simultaneously with the CA 1.23 m (red points) and the IAC 80 cm (empty orange circles) telescopes. The data of the two telescopes are superimposed to highlight the difference in the light-curve shape caused by the different filter adopted (Knutson et al. 2007). The dashed vertical line represents the time of transit mid-point that, thanks to the two-site strategy, was very accurately measured.

physically realistic model. As in previous cases (Mancini et al. 2013b, 2014; Mohler-Fischer et al. 2013), we utilise the PRISM[4] and GEMC[5] codes (Tregloan-Reed et al. 2013, 2015) to undertake this task. PRISM performs a modelling of planetary-transit light curves with one or more starspots by means of a pixellation approach in Cartesian coordinates. GEMC uses a differential evolution Markov chain Monte Carlo (DE-MCMC) approach to locate the parameters of the PRISM model that better fit the data, using a global search. The fitted parameters of PRISM are the sum and ratio of the fractional radii[6] ($r_A + r_b$ and $k = \frac{r_b}{r_A}$), the orbital period and inclination (P and i), the time of transit midpoint (T_0) and the coefficients of the quadratic limb darkening law (u_A and v_A).

The PRISM+GEMC code works in the way that the user has to decide how many starspots have to be fitted. We fitted for all the spot anomalies that can be seen in the transit light curves. Each starspot is then reproduced by the longitude and co-latitude of its centre (θ and ϕ), its angular radius (r_{spot}), and its contrast (ρ_{spot}), the last being the ratio of the surface brightness of the starspot to that of the surrounding photosphere. The orbital eccentricity was fixed to zero (Bakos et al. 2012).

The derived parameters of the planetary system are reported in Table 3, while those of the starspots in Table 4. The light

curves and their best-fitting models are shown in Fig. 3. For each transit, a representation of the starspots on the stellar disc is drawn in Fig. 8.

The light curves for the WASP-11/HAT-P-10 transits were modelled by JKTEBOP[7] (see Southworth 2008, 2013 and references therein), because this code is much faster than the previous one, and no clear starspot anomalies are visible. The parameters used for JKTEBOP were the same as for PRISM, and the orbital eccentricity was also fixed to zero (Bakos et al. 2009). Light curves from the second discovery paper (Bakos et al. 2009) were also reanalysed. The results of the fits are summarised in Table 5 and displayed in Fig. 4. Its low quality meant that the *Cassini* light curve (top curve in Fig. 4) was excluded from the analysis.

3.1. Orbital period determination

We used the new photometric data to refine the transit ephemeris of HAT-P-36 b. The transit times and uncertainties were obtained using PRISM+GEMC as previously explained. To these timings, we added four from the discovery paper (Bakos et al. 2012) and two from Maciejewski et al. (2013)[8]. The nine timings were placed on the BJD(TDB) time system (Table 6). The resulting measurements of transit midpoints were fitted with a straight line to obtain a final orbital ephemeris

$$P = 1.32734684 \pm 0.00000050 \,\mathrm{d}$$

and the mid-transit time at cycle zero

$$T_0 = 2\,455\,565.18165 \pm 0.00037 \,\mathrm{BJD(TDB)},$$

with reduced $\chi_\nu^2 = 2.5$, which is significantly greater than unity. A plot of the residuals around the fit (see Fig. 6) does not indicate any clear systematic deviation from the predicted transit times.

We introduced other 21 timings in the analysis measured based on transit light curves observed by amateur astronomers and available on the ETD[9] website. These 21 light curves were selected considering if they had complete coverage of the transit and a data quality index ≤ 3. Repeating the analysis with a larger sample we obtained 4.1 as the reduced χ_ν^2 of the fit. A high value of χ_ν^2 means that the assumption of a constant orbital period does

---

[4] Planetary Retrospective Integrated Star-spot Model.
[5] Genetic Evolution Markov Chain.
[6] The fractional radii are defined as $r_A = \frac{R_\star}{a}$ and $r_b = \frac{R_p}{a}$, where $R_\star$ and R_p are the true radii of the star and planet, and a is the orbital semimajor axis.

[7] JKTEBOP is written in FORTRAN77 and is available at: http://www.astro.keele.ac.uk/jkt/codes/jktebop.html
[8] We added 1/25 days to the published values to correct an error caused by a misunderstanding in reading the time stamps of the fits files.
[9] The Exoplanet Transit Database (ETD) website can be found at http://var2.astro.cz/ETD

Table 3. Photometric properties of the HAT-P-36 system derived by fitting the light curves with GEMC.

Source	Filter	$r_A + r_b$	k	$i°$	u_A	v_A
Cassini 1.52 m	Gunn r	0.2278 ± 0.0037	0.1243 ± 0.0025	85.95 ± 0.34	0.24 ± 0.13	0.40 ± 0.21
CA 1.23 m #1	Cousins I	0.2298 ± 0.0039	0.1290 ± 0.0023	85.76 ± 0.36	0.25 ± 0.10	0.29 ± 0.19
CA 1.23 m #2	Cousins I	0.2285 ± 0.0039	0.1298 ± 0.0012	85.86 ± 0.43	0.32 ± 0.11	0.15 ± 0.14

Table 4. Starspot parameters derived from the GEMC fitting of the HAT-P-36 transit light curves presented in this work.

Telescope	Starspot	$\theta(°)^a$	$\phi(°)^b$	$r_{spot}(°)^c$	$\rho_{spot}{}^d$	Temperature (K)^e
Cassini 1.52 m	#1	−36.59 ± 1.85	77.41 ± 5.82	11.42 ± 3.45	0.65 ± 0.07	5070 ± 129
	#2	38.29 ± 2.88	82.68 ± 5.27	12.54 ± 5.57	0.62 ± 0.23	5016 ± 421
CA 1.23 m #1	#1	21.06 ± 3.20	86.52 ± 3.96	17.67 ± 4.81	$0.86^{+0.14}_{-0.17}$	5380 ± 305
CA 1.23 m #2	#1	−24.99 ± 4.91	87.08 ± 3.17	21.38 ± 6.82	$0.92^{+0.08}_{-0.14}$	5485 ± 244
	#2	46.00 ± 14.13	88.27 ± 2.38	18.66 ± 3.52	0.78 ± 0.19	5253 ± 353

Notes. $^{(a)}$ The longitude of the centre of the spot is defined to be 0° at the centre of the stellar disc and can vary from −90° to 90°. $^{(b)}$ The co-latitude of the centre of the spot is defined to be 0° at the north pole and 180° at the south pole. $^{(c)}$ Angular radius of the starspot (note that an angular radius of 90° covers half of stellar surface). $^{(d)}$ Spot contrast; note that 1.0 equals the brightness of the surrounding photosphere. $^{(e)}$ The temperature of the starspots are obtained by considering the photosphere and the starspots as black bodies.

Table 5. Photometric properties of the WASP-11/HAT-P-10 system derived by fitting the light curves with JKTEBOP.

Source	Filter	$r_A + r_b$	k	$i°$	u_A	v_A
Cassini 1.52 m	Gunn r	0.10137 ± 0.01380	0.13639 ± 0.00868	88.00 ± 1.97	0.56 ± 0.23	0.21 ± 0.06
CA 1.23 m	Cousins I	0.09230 ± 0.00197	0.13234 ± 0.00078	89.09 ± 0.68	0.24 ± 0.04	0.25 ± 0.07
IAC 80 cm	Cousins R	0.09695 ± 0.00358	0.13657 ± 0.00200	88.29 ± 0.54	0.40 ± 0.08	0.21 ± 0.07
FLWO 1.2 m	Sloan z	0.09277 ± 0.00350	0.12818 ± 0.00181	89.95 ± 0.92	0.41 ± 0.06	0.27 ± 0.07
FLWO 1.2 m	Sloan i	0.09160 ± 0.00242	0.12856 ± 0.00156	89.94 ± 0.76	0.49 ± 0.05	0.25 ± 0.07

Table 6. Times of transit midpoint of HAT-P-36 b and their residuals.

Time of minimum BJD(TDB)−2 400 000	Cycle no.	O−C (JD)	Reference
55 555.89060 ± 0.00043	−7	0.000376	1
55 597.04088 ± 0.00770	24	0.002904	1
55 601.01882 ± 0.00074	27	−0.001197	1
55 608.98390 ± 0.00030	33	−0.000198	1
56 365.56800 ± 0.00234	603	−0.001928	3
56 397.42170 ± 0.00202	627	−0.004655	3
56 397.42894 ± 0.00031	627	0.000822	2
56 762.44834 ± 0.00018	902	−0.000158	3
56 766.43055 ± 0.00028	905	−0.000011	3

References. (1) FLWO 1.2 m (Bakos et al. 2012); (2) *Cassini* 1.52 m (this work); (3) CA 1.23 m (this work).

Table 7. Times of transit midpoint of WASP-11/HAT-P-10 b and their residuals.

Time of minimum BJD(TDB)−2 400 000	Cycle no.	O−C (JD)	Reference
54 729.90657 ± 0.00023	0	−0.000589	1
54 770.85432 ± 0.00011	11	−0.000115	1
54 793.19692 ± 0.00076	17	0.002071	2
55 143.10895 ± 0.00046	111	0.001013	2
55 161.71529 ± 0.00021	116	0.000490	3
55 507.90419 ± 0.00042	209	−0.001219	3
55 842.92921 ± 0.00021	299	0.000631	3
55 842.92952 ± 0.00044	299	0.000941	3
55 865.26734 ± 0.00166	305	−0.001483	2
55 150.54662 ± 0.00104	113	−0.000741	4
56 933.61504 ± 0.00008	592	−0.000086	5
56 933.61522 ± 0.00018	592	0.000099	6

References. (1) FLWO 1.2 m (Bakos et al. 2009); (2) Wang et al. (2014); (3) Sada et al. (2012); (4) *Cassini* 1.52 m (this work); (5) CA 1.23 m (this work); (6) IAC 80 cm (this work).
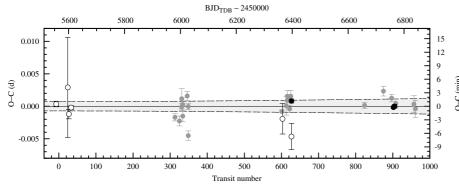
not agree with the timing measurements. This could indicate either transit timing variations (TTVs) or that the measurement errors are underestimated. The latter possibility can occur very easily, but be difficult to rule out, so the detection of TTVs requires more than just an excess χ^2_ν. The Lomb-Scargle periodogram generated for timing residuals shows no signicant signal, making any periodic variation unlikely, so we do not claim the existence of TTVs in this system. The residuals of the ETD timings are also shown in Fig. 6 for completeness.

New mid-transit times (three transits; this work) and those available in the literature (9 transits) allowed us to refine transit ephemeris for WASP-11/HAT-P-10 b too. In particular, the two light curves from Bakos et al. (2009) were refitted with JKTEBOP (Fig. 4). All the timings are summarised in Table 7. As a result of a linear fit, in which timing uncertainties were taken as weights,

we derived

$$P = 3.72247967 ± 0.00000045 \text{ d}$$

and the mid-transit time at cycle zero

$$T_0 = 2\,454\,729.90716 ± 0.00020 \text{ BJD}_{TDB},$$

with $\chi^2_\nu = 5.0$, which is again far from unity. This could be explained again by underestimated timing uncertainties or hypothesizing a variation in transit times caused by unseen planetary companion or stellar activity. However, also for this case the
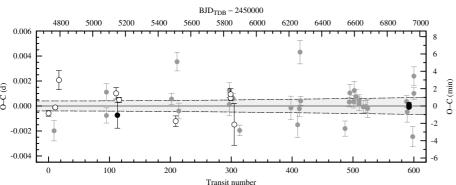
Fig. 6. Residuals for the timings of HAT-P-36 b at mid-transit versus a linear ephemeris. The four timings reported by Bakos et al. (2012) and the two by Maciejewski et al. (2013) are plotted using empty circles, while those marked with grey circles are from ETD. The timings measured by this work are shown with black circles. The dashed lines mark 2σ uncertainties of the ephemeris (i.e. at the 95% confidence level), which was estimated without considering the data from ETD.

Fig. 7. Residuals for the timings of WASP-11/HAT-P-10 b at mid-transit versus a linear ephemeris. The filled black dots are from this work, open circles from the literature, (i.e. Bakos et al. 2009; Sada et al. 2012; Wang et al. 2014), and grey dots from ETD. The dashed lines mark 2σ uncertainties of the ephemeris, which was estimated without considering the data from ETD.

Lomb-Scargle periodogram shows no significant signal, not supporting the second hypothesis. The plot of the residuals around the fit is shown in Fig. 7.

As in the previous case, we selected 34 transits from ETD, using the same criteria as explained above. Most of the corresponding timings are very scattered around the predicted transit mid-times, but have tiny error bars. Including them in the fit returns a higher value for the χ_ν^2, suggesting that their uncertainties are very underestimated, and the data reported on ETD should be used cautiously. They are shown in Fig. 7.

We would like to stress, however, that since in both cases, the timing measurements are in groups separated by several hundred days, we are not sensitive to all the periodicities. Only by performing systematic observations of many subsequent transits is it possible to rule out the presence of additional bodies in the two TEP systems with higher confidence.
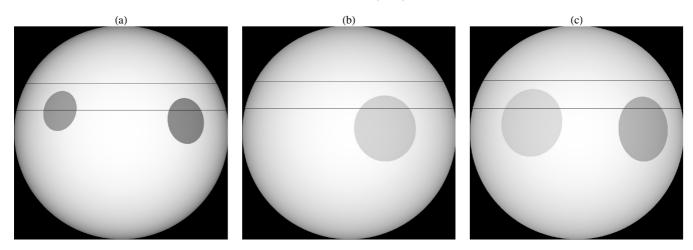
3.2. HAT-P-36 starspots

As described in Sect. 3, the anomalies in the three HAT-P-36 light curves were modelled as starspots, whose parameters were fitted with those of the transits (see Tables 3 and 4). The stellar disc, the positions of starspots and the transit chords are displayed in Fig. 8, based on the results of the modelling. Considering both the photosphere and the starspots as black bodies (Rabus et al. 2009; Sanchis-Ojeda et al. 2011; Mohler-Fischer et al. 2013) and using Eq. (1) of Silva (2003) and $T_{\rm eff} = 5620 \pm 40$ (see Sect. 4.1), we estimated the temperature of the starspots at different bands and reported them in the last column of Table 4. The values of the starspot temperature estimated in the transit on 2013 April are in good agreement with each other within the experimental uncertainties. The same is true for those observed in the two transits on 2014 April, even if they point to starspots with temperatures higher than, but still compatible, with those of the previous year. The starspot temperatures measured from the Loiano and CAHA observations are consistent

with what has been measured for other main-sequence stars in transit observations, as we can see from Fig. 9, where we report the starspot temperature contrast versus the temperature of the photosphere of the corresponding star for data taken from the literature. The spectral class of the stars is also reported and allows us to figure out that the temperature difference between photosphere and starspots does not strongly depend on spectral type, as already noted by Strassmeier (2009).
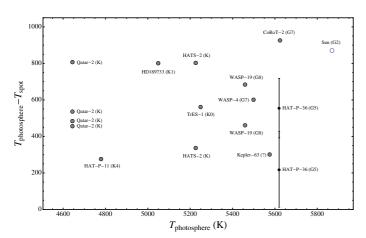
The observations of multiple planetary transits across the same starspot or starspot complex could provide another type of precious information (Sanchis-Ojeda et al. 2011). Indeed, thanks to the good alignment between the stellar spin axis and the perpendicular to the planet's orbital plane, one can measure the shift in position of the starspot between the transit events and constrain the alignment between the orbital axis of the planet and the spin axis of the star with higher precision than from the measurement of the RM effect (e.g., Tregloan-Reed et al. 2013).

In our case, we have observed two consecutive transits in 2014 April 14 and 18, and we might wonder if the planet had crossed the same starspot complex in those transit events. According to Eq. (1) of Mancini et al. (2014), the same starspot can be observed after consecutive transits or after some orbital cycles, presuming that in the latter case, the star performs one or more rotations around its axis. Since the projected obliquity measured by the RM effect (see Sect. 4) indicates spin-orbit alignment, we expect to find similar values for the starspot parameters in our fits. Examining Table 4, we note that they seem to agree on co-latitude, size, and contrast within their 1σ errors. Owing to its size, the starspot on April 14 should still be seen four days later (if it is on the visible side of the star). That means that the starspot should have travelled ~315° in four days giving a rotation period of ~4.57 days, which is too fast compared with that at the stellar equator estimated from the sky-projected rotation rate and the stellar radius, that is,

$$P_{\rm rot} \approx \frac{2\pi R_\star}{v \sin i_\star} \sin i_\star = (16.9 \pm 4.3 \,{\rm d}) \sin i_\star, \qquad (1)$$

(a)   (b)   (c)

Fig. 8. Representation of the stellar disc, starspot positions, and transit chord for the three HAT-P-36 datasets containing spot anomalies: **a)** refers to the transit observed with the *Cassini* 1.52 m telescope on 2013 April 15, and **b)** and **c)** to those observed with the CA 1.23 m telescope on 2014 April 14 and 18, respectively. The grey scale of each starspot is related to its contrast (compare with values in Table 4).

Fig. 9. Starspot temperature contrast with respect to the photospheric temperature in several dwarf stars. The name and spectral type of the star are also reported. The values for TrES-1, CoRoT-2, HD 189733, WASP-4, HATS-2, Kepler-63, Qatar-2 are taken from Rabus et al. (2009), Silva-Valio et al. (2010), Sing et al. (2011), Sanchis-Ojeda et al. (2011), Mohler-Fischer et al. (2013), Sanchis-Ojeda et al. (2013), Mancini et al. (2014), respectively. The two values for WASP-19 are from Mancini et al. (2013b) and Huitson et al. (2013). The value of the Sun was taken from Berdyugina (2005). The error bars have been suppressed for clarity. Note that some stars appear twice or more. The black dots refer to the values estimated for the case of HAT-P-36 (this work). In particular, the lower is the value estimated by taking the weighted mean from the starspots detected with the *Cassini* telescope in April 2013, while the higher value was calculated from starspots detected with the CA 1.23 m telescope in April 2014.

where $i_\star$ is the inclination of the stellar rotation axis with respect to the line of sight. If we consider reversing the rotational direction so that the starspot is travelling right to left, then the starspot had to travel for ~45° in four days; but this implies that the stellar rotation period at co-latitude of 87° would now be too long (~32 days) and that HAT-P-36 b has a retrograde orbit. Since the latter hypothesis is excluded by the geometry of the RM effect that we observed (see Sect. 4.3) and since four days are not sufficient for the starspot to rotate around the back of the star and then appear on the left hemisphere, we conclude that the starspot observed on 2014 April 14 is different from those on April 18.

3.3. Frequency analysis of the time-series light curves

In addition to the new photometric measurements of the transits presented in this work, dense time-series light curves are available in the WASP and HAT archives/databases for both the stars. These data are potentially very useful for detecting the signatures of the rotational period of each of the two stars. This is particularly true for the case of HAT-P-36, since the starspots detected in the photometric light curves (see previous section) indicate that this star is active. A further confirmation of this activity is also given by the spectral analysis, as seen in Sect. 4.2.
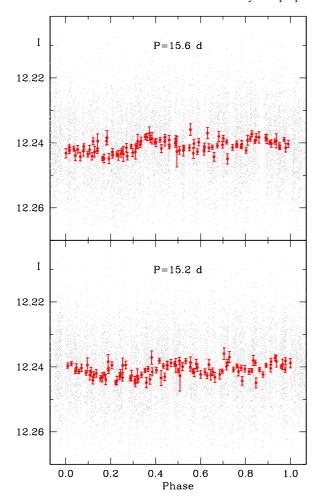
We retrieved the photometric time series for HAT-P-36 (SDSS r filter) and WASP-11/HAT-P-10 (I Bessel filter) from the HAT public archive[10]; more specifically, we used the magnitudes data sets tagged as TF1 (Kovács et al. 2005). The WASP data available for WASP-11/HAT-P-10 were downloaded from the NASA Exoplanet Archive[11]. The in-transit data points were removed from the light curve of each dataset.

The frequency analysis of the WASP and HAT time-series data related to WASP-11/HAT-P-10 did not detect any significant periodicity. Only the HAT data show a non-significant peak at $f = 0.034$ d^{-1}. It is close to the synodic month, and the folded light curve shows a gap in the phase coverage corresponding to the Full Moon epochs. Therefore, it has been recognised as a spurious peak due to a combination of instrumental effects and spectral window.

On the other hand, the analysis of the HAT time-series light curve of HAT-P-36 (see Fig. 10) provided more interesting results. After removing the transit data, the time-series light curve is composed of 9891 measurements. Both the iterative sine-wave fitting method (ISWF; Vaniĉek 1971) and the Lomb-Scargle periodogram supplied a lower peak at $f = 0.066$ d^{-1} and a higher one at $2f = 0.13$ d^{-1}. Figure 11 shows the power spectrum obtained with the ISWF method. The amplitudes of the $2f$ and f components are 1.40 ± 0.15 and 0.88 ± 0.15 mmag, respectively. Since the level of the noise is 0.2 mmag, both are greater than the $S/N = 4.0$ significance threshold (Kuschnig et al. 1997). Moreover, the harmonics $3f$ and $4f$ are both clearly visible, the latter being more relevant than the former. HAT-P-36 was measured several times per night and often over night. We could thus calculate 97 night averages (Fig. 10). The frequency
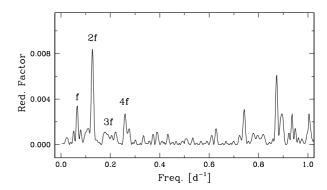

Fig. 10. *Top panel*: single measurements (grey dots) and average values on single nights (red circles with errorbars) folded with $P = 15.6$ d, the best period obtained fitting the data with f and $2f$ fixed. *Bottom panel*: single measurements (grey dots) and average values (red circles with errorbars) folded with $P = 15.2$ d, the best period obtained leaving the frequencies free to vary.

Fig. 11. Power spectrum of the original data of HAT-P-36, after removing the measurements during transit events.

4. HARPS-N spectra analysis

4.1. Spectroscopic determination of stellar atmospheric parameters

The effective temperature (T_{eff}), surface gravity ($\log g_\star$), iron abundance ([Fe/H]) and microturbulence velocity (v_{mic}) of the two host stars were derived by using the spectral analysis package MOOG (Sneden 1973, version 2013), and the equivalent widths (EWs) of iron lines, as described in detail in Biazzo et al. (2012). The EWs were measured on the mean spectrum obtained by averaging all the HARPS-N spectra available for each of the two stars. Here, T_{eff} was determined by imposing the condition that the Fe I abundance does not depend on the excitation potential of the lines, the microturbulence velocity, by requiring that the Fe I abundance is independent of the line EWs, and $\log g_\star$ by the Fe I/Fe II ionisation equilibrium condition. The results are reported in Tables 8 and 9 for HAT-P-36 and WASP-11, respectively. The projected rotational velocity was estimated by means of spectral synthesis analysis with MOOG, yielding $v \sin i_\star$ values of 3.0 ± 0.5 km s^{-1} and 0.9 ± 0.5 km s^{-1} for HAT-P-36 and WASP-11, respectively, which are consistent, within the errors, with those obtained from the RM effect modelling (see Sect. 4.3).

4.2. Stellar activity index

The median values of the stellar activity index estimated from the HARPS-N spectra turned out to be $\log R'_{HK} = -4.636 \pm 0.066$ dex for HAT-P-36 and -4.848 ± 0.029 dex for WASP-11/HAT-P-10, indicating moderate and low activity, respectively (e.g. Noyes et al. 1984). These values agree with what we have found in Sect. 3.3 by analysing the big photometric data sets from the HATNet amd WASP surveys. The above values were obtained by adopting $B - V = 0.719$ and 0.989, respectively, based on the stellar effective temperature and the colour-T_{eff} conversion table by Casagrande et al. (2010). Knutson et al. (2010) find $\log R'_{HK} = -4.823$ dex for WASP-11/HAT-P-10 (estimated considering $B - V = 1.01$), which is in good agreement with our value.

Thanks to the activity index, we can also assess the expected rotation period from the level of the stellar activity, obtaining $P_{rot} = 18.3 \pm 3.1$ d and 18.7 ± 2.9 d for HAT-P-36 using Noyes et al. (1984) and Mamajek & Hillenbrand (2008) calibration scales, respectively, in quite good agreement, within the observational uncertainties, with what was estimated in Sect. 3.3. For WASP-11/HAT-P-10, we obtained 40.8 ± 1.8 d and 40.9 ± 2.2 d, respectively.

analysis of these averages supplied the same results as the single measurements.

When the even harmonics have amplitudes larger than those of the odd ones, the resulting light curve is shaped as a double wave. Since we know that the star is seen equator-on (see Sect. 4.3), such a light curve can easily be due to two groups of spots that are alternatively visible to the observer. This is an independent confirmation of the spot model suggested in the previous section. We determined the rotational period in two ways. First, we searched for the best fit by fixing the frequency f and its harmonic $2f$. This procedure yields $P_{rot} = 15.2 \pm 0.3$ d. Then, we supposed that the differential rotation and the spread in longitude did not justify this condition, so we left the two frequency values free to vary, obtaining $P_{rot} = 15.6 \pm 0.1$ d. The periods are the same within the error bars and in excellent agreement with the period inferred from the stellar parameters, see Eq. (1). We merged the two determinations into $P_{rot} = 15.3 \pm 0.4$ d to cover both values and respective error bars. The HAT-P-36 light curve is shown in Fig. 10, phase-folded with $P_{rot} = 15.6$ (top panel) and $P_{rot} = 15.2$ (bottom panel) days.

Table 8. Physical parameters of the planetary system HAT-P-36 derived in this work.

Parameter	Nomen.	Unit	This work	Bakos et al. (2012)
Stellar parameters				
Spectral class			G5 V	...
Effective temperature	$T_{\rm eff}$	K	5620 ± 40	5560 ± 100
Metal abundance	[Fe/H]		$+0.25 \pm 0.09$	$+0.26 \pm 0.10$
Projected rotational velocity	$v \sin i_\star$	km s^{-1}	3.12 ± 0.75	3.58 ± 0.5
Rotational period	$P_{\rm rot}$	days	15.3 ± 0.4	...
Linear LD coefficient	u		0.81 ± 0.17	...
Mass	$M_\star$	$M_\odot$	$1.030 \pm 0.029 \pm 0.030$	1.022 ± 0.049
Radius	$R_\star$	$R_\odot$	$1.041 \pm 0.013 \pm 0.010$	1.096 ± 0.056
Mean density	$\rho_\star$	$\rho_\odot$	0.913 ± 0.027	...
Logarithmic surface gravity	$\log g_\star$	cgs	$4.416 \pm 0.010 \pm 0.004$	4.37 ± 0.04
Age		Gyr	$4.5^{+2.4}_{-1.4}{}^{+3.1}_{-2.8}$	$6.6^{+2.9}_{-1.8}$
Planetary parameters				
Mass	$M_{\rm p}$	$M_{\rm Jup}$	$1.852 \pm 0.088 \pm 0.036$	1.832 ± 0.099
Radius	$R_{\rm p}$	$R_{\rm Jup}$	$1.304 \pm 0.021 \pm 0.013$	1.264 ± 0.071
Mean density	$\rho_{\rm p}$	$\rho_{\rm Jup}$	$0.737 \pm 0.095 \pm 0.007$	0.84 ± 0.14
Surface gravity	$g_{\rm p}$	m s^{-2}	27.0 ± 1.4	28 ± 3
Equilibrium temperature ...	$T_{\rm eq}$	K	1788 ± 15	1823 ± 55
Safronov number	Θ		$0.0658 \pm 0.0030 \pm 0.0006$	0.067 ± 0.005
Orbital parameters				
Time of mid-transit	T_0	BJD(TDB)	$2\,455\,565.18167 \pm 0.00036$	$2\,455\,565.18144 \pm 0.00020$
Period	$P_{\rm orb}$	days	$1.32734683 \pm 0.00000048$	1.327347 ± 0.000003
Semi-major axis	a	au	$0.02388 \pm 0.00022 \pm 0.00023$	0.0238 ± 0.0004
Inclination	i	degree	85.86 ± 0.21	86.0 ± 1.3
RV-curve semi-amplitude ..	$K_{\rm A}$	m s^{-1}	316 ± 39^a	334.7 ± 14.5
Barycentric RV	γ	km s^{-1}	-16.327 ± 0.006	-16.29 ± 0.10
Projected spin-orbit angle ..	λ	degree	-14 ± 18	...
True spin-orbit angle	ψ	degree	<63	...

Notes. Where two errorbars are given, the first refers to the statistical uncertainties and the second to the systematic errors. [a] This value of $K_{\rm A}$ was determined from our RV data, which were taken during transit time only. The value reported by Bakos et al. (2009), which is based on RV data with a much better coverage of the orbital phase, was therefore preferred for the determination of the other physical parameters of the system (see Sect. 5).

Finally, we can get a clue to stellar age by applying the activity-age calibration proposed by Mamajek & Hillenbrand (2008), obtaining 2 Gyr and 5 Gyr for HAT-P-36 and WASP-11/HAT-P-10, respectively. However, we notice that the ages derived from stellar rotation and activity could be altered in the TEP systems because of star-planet tidal interactions, and any discrepancy with the values derived from the isochrones (see Sect. 5) may be due to this.

4.3. Determination of the spin-orbit alignment

The analysis of the photometric data allowed us a direct measurement, without reliance on theoretical stellar models, of the stellar mean density, $\rho_\star$ (Seager & Mallén-Ornelas 2003; Sozzetti et al. 2007) and, in combination with the spectroscopic orbital solution, the planetary surface gravity, $g_{\rm p}$ (Southworth et al. 2007), for each system. Exploiting the measured values of $\rho_\star$, $T_{\rm eff}$ and [Fe/H], we made use of the Yonsei-Yale evolutionary tracks (Demarque et al. 2004) to determine stellar characteristics, including $M_\star$ and $R_\star$. The HARPS-N RV data sets were then fitted using a model that accounts both for the RV orbital trend and the RM anomaly. We used the RM model that we elaborated and described in Covino et al. (2013) and Esposito et al. (2014), and we used the same least-square minimisation to adjust it to the data. We set as free the barycentric radial velocity, γ, the mass of the planet, $M_{\rm p}$, the projected stellar rotational velocity, $v \sin i_\star$, the projected spin-orbit angle, λ and the linear limb-darkening coefficient u. All the other relevant parameters were kept fixed to the values determined

from the spectroscopic and light curves analysis. The best-fitting RV models are illustrated in Figs. 1 and 2, superimposed on the datasets. In particular, the sky-projected spin-orbit misalignment angle was $\lambda = -14 \pm 18$ deg for HAT-P-36 and $\lambda = 7 \pm 5$ deg for WASP-11/HAT-P-10, indicating an alignment of the stellar spin with the orbit of the planet for both the systems. The final error bars were computed by a bootstrapping approach. The greater uncertainty in HAT-P-36 is of course because the transit was not completely observed. The reduced χ^2_ν maps in the $\lambda - v \sin i_\star$ plane do not point to any clear correlation between λ and $v \sin i_\star$.

The precise knowledge of the rotational period of a star, allows estimating the stellar spin inclination angle, $i_\star$, and thus the true spin-orbit alignment angle, ψ. This is exactly the case for HAT-P-36, for which the analysis of the long time-series data set recorded by HATNet survey allowed us to determine the stellar rotational period. By using $P_{\rm rot} = 15.3 \pm 0.4$ d (Sect. 3.3), we estimated that $i_\star = 65° \pm 34°$. Then, we used Eq. (7) in Winn et al. (2007),

$$\cos\psi = \cos i_\star \cos i + \sin i_\star \sin i \cos \lambda, \qquad (2)$$

to derive the true misalignment angle, obtaining an upper limit of $\psi < 63$. The major source of error in the determination of both $i_\star$ and ψ, estimated through the propagation of uncertainties, comes from the large relative error in the measurement of $v \sin i_\star$; the observation of a full transit would have reduced the errors by a factor of 2 or more.

Table 9. Physical parameters of the planetary system WASP-11/HAT-P-10 derived in this work.

Parameter	Nomen./Unit	This work	West et al. (2009)	Bakos et al. (2009)	Wang et al. (2014)
Stellar parameters					
Spectral class		K3 V	K	K	...
Effective temperature	$T_{\rm eff}$ (K)	4900 ± 65	4800 ± 100	4980 ± 60	...
Metal abundance	[Fe/H]	$+0.12 \pm 0.09$	$+0.0 \pm 0.2$	$+0.13 \pm 0.08$	...
Proj. rotational velocity ...	$v \sin i_\star$ (km s^{-1})	1.04 ± 0.15	<6.0	0.5 ± 0.2	...
Linear LD coefficient	u	0.78 ± 0.16	...	...	...
Mass	$M_\star$ ($M_\odot$)	$0.806 \pm 0.038 \pm 0.013$	$0.77^{+0.10}_{-0.08}$	0.83 ± 0.03	0.862 ± 0.014
Radius	$R_\star$ ($R_\odot$)	$0.772 \pm 0.014 \pm 0.004$	$0.74^{+0.04}_{-0.03}$	0.79 ± 0.02	$0.784^{+0.018}_{-0.011}$
Mean density	$\rho_\star$ ($\rho_\odot$)	1.748 ± 0.074	...	...	$1.789^{+0.072}_{-0.116}$
Logarithmic surface gravity	$\log g_\star$ (cgs)	$4.569 \pm 0.018 \pm 0.002$	4.45 ± 0.20	4.56 ± 0.02	...
Age	(Gyr)	$7.6^{+5.8+1.6}_{-3.0-1.8}$	...	7.9 ± 3.8	...
Planetary parameters					
Mass	$M_{\rm p}$ ($M_{\rm Jup}$)	$0.492 \pm 0.023 \pm 0.005$	0.53 ± 0.07	0.487 ± 0.018	0.526 ± 0.019
Radius	$R_{\rm p}$ ($R_{\rm Jup}$)	$0.990 \pm 0.022 \pm 0.005$	$0.91^{+0.06}_{-0.03}$	$1.005^{+0.032}_{-0.027}$	$0.999^{+0.029}_{-0.018}$
Mean density	$\rho_{\rm p}$ ($\rho_{\rm Jup}$)	$0.475 \pm 0.026 \pm 0.002$	$0.69^{+0.07}_{-0.11}$	0.594 ± 0.052	$0.526^{+0.035}_{-0.046}$
Surface gravity	$g_{\rm p}$ (m s^{-2})	12.45 ± 0.50	$14.45^{+1.66}_{-1.33}$	12.02 ± 0.83	...
Equilibrium temperature ..	$T_{\rm eq}$ (K)	992 ± 14	960 ± 70	1020 ± 17	$1006.5^{+16.4}_{-14.6}$
Safronov number	Θ	$0.0539 \pm 0.0019 \pm 0.0003$	...	0.053 ± 0.002	...
Orbital parameters					
Time of mid-transit	T_0 (BJD$_{\rm TDB}$)	2 454 729.90716 ± 0.00020	2 454 473.05588 ± 0.00020	2 454 759.68683 ± 0.00016	2 454 808.07904 ± 0.00012
Period	$P_{\rm orb}$ (days)	3.72247967 ± 0.00000045	3.722465 ± 0.000007	3.7224747 ± 0.0000065	3.72247669 ± 0.00000181
Semi-major axis	a (au)	0.04375 $\pm 0.00070 \pm 0.00023$	0.043 ± 0.002	0.0435 ± 0.0006	0.04473 ± 0.00024
Inclination	i (degree)	89.03 ± 0.34	$89.8^{+0.2}_{-0.8}$	$88.6^{+0.5}_{-0.4}$	$89.138^{+0.503}_{-0.470}$
RV curve semi-amplitude .	$K_{\rm A}$ (m s^{-1})	82.7 ± 4.2 [a]	82.1 ± 7.4	74.5 ± 1.8	$76.16^{+2.67}_{-2.58}$
Barycentric RV	γ (km s^{-1})	4.8951 ± 0.0021	4.9077 ± 0.0015	3.95 ± 0.43	...
Proj. spin-orbit angle	λ (degree)	7 ± 5	...	...	...

Notes. Where two errorbars are given, the first refers to the statistical uncertainties and the second to the systematic errors. [a] This value of $K_{\rm A}$ was determined from our RV data, which were taken during transit time only. The value reported by Bakos et al. (2009), which is based on RV data with a much better coverage of the orbital phase, was therefore preferred for the determination of the other physical parameters of the system (see Sect. 5).

5. Physical parameters of the two systems

For calculating the full physical properties of each planetary system, we used the HSTEP methodology (see Southworth 2012, and references therein). The values of the photometric parameters $r_{\rm A} + r_{\rm b}$, k and i were first combined into weighted means. The orbital eccentricity was fixed to zero. We added in the measured P from the light curve analysis, $T_{\rm eff}$ and [Fe/H] from the spectroscopic analysis, and the velocity semi-amplitude of the star, $K_{\rm A}$, measured from the RVs. For $K_{\rm A}$ we used the values from Bakos et al. (2012, 2009). These come from spectra with reasonable coverage of the orbits of the host stars, so are more precise than our own values, which come from data obtained only during or close to transit. We estimated a starting value for the velocity semi-amplitude of the planet, $K_{\rm p}$, and used this to determine a provisional set of physical properties of the system using standard formulae (e.g., Hilditch 2001).

We then interpolated within a set of tabulated predictions from a theoretical stellar model to find the expected stellar radius and $T_{\rm eff}$ for our provisional mass and the observed [Fe/H]. The value of $K_{\rm p}$ was then iteratively refined to maximise the agreement between the observed and predicted $T_{\rm eff}$, and the provisional $(R_{\rm A} + R_{\rm b})/a$ and measured $r_{\rm A} + r_{\rm b}$ values. This $K_{\rm b}$ was then used alongside the other quantities given above to determine the physical properties of the system. This process was performed over all possible ages for the stars, from the zero-age
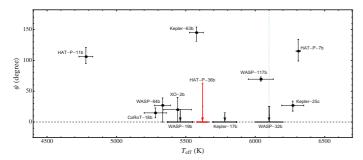
to the terminal-age main sequence, and the overall best-fitting age and resulting physical parameters found.

The above process was performed using each of five different sets of theoretical models: Claret (Claret 2004), Y^2 (Demarque et al. 2004), BaSTI (Pietrinferni et al. 2004), VRSS (VandenBerg et al. 2006), and DSEP (Dotter et al. 2008). The final result of this analysis was five sets of properties for each system, one from each of the five sources of theoretical models (see Tables A.1 and A.2). For the final value of each output parameter, we calculated the unweighted mean of the five estimates from using the different sets of model predictions. Statistical errorbars were propagated from the errorbars in the values of all input parameters. Systematic errorbars were assigned based on the inter-agreement between the results from the five different stellar models.

Tables 8 and 9 give the physical properties we found for HAT-P-36 and WASP-11, respectively. Our results are in good agreement, but they are more precise than previous determinations.

6. Summary and conclusions

In the framework of the GAPS programme, we are observing a sample of TEP systems hosting close-in hot Jupiters with the HARPS-N spectrograph. The goal is to measure their spin-orbit alignment (by observing the RM effect) and study whether this quantity is correlated with other physical properties. Here,

Fig. 12. True orbital obliquity as a function of the effective stellar temperature for 12 TEP systems. Data taken from TEPCat. The red point indicates the location of HAT-P-36 (this work). Arrows indicate 1σ upper limits. The green-dotted line separates the cool TEP systems from those with $T_{\rm eff} > 6100$ K (Dawson 2014).

we have presented an exhaustive study of the HAT-P-36 and WASP-11/HAT-P10 planetary systems, based on data collected with four telescopes during transit events.

By analysing these new photometric and spectroscopic data, we revised the physical parameters of the two planetary systems, finding that previous determinations agree with our more accurate results, within the uncertainties.

Interestingly, we observed anomalies in three photometric transit light curves of HAT-P-36 that, after appropriate modelling, turned out to be compatible with starspot complexes on the photosphere of the star. The main characteristics of the starspots were estimated and compared with those observed in other TEP systems. The HAT-P-36 starspot activity is confirmed by analysis of the HARPS-N spectra, which gives a stellar activity index of $\log R'_{\rm HK} = -4.65$ dex, and by study of the whole photometric data set collected by the HATNet survey. The frequency analysis of this time-series data revealed a clear modulation in the light curve caused by starspots, allowing us to get an accurate measurement of the rotational period of the star, $P_{\rm rot} = 15.3 \pm 0.4$ days. A similar study, performed for WASP-11/HAT-P-10 on both the WASP and HATNet survey light curves, did not highlight any clear photometric modulation.

The RM effect was partially covered in HAT-P-36 (because of bad weather conditions) and wholly observed in WASP-11/HAT-P-10. Thanks to the high-resolution HARPS-N spectra, the sky projection of the orbital obliquity was successfully measured for both the systems, indicating a good spin-orbit alignment.

Based on a recent gyrochronology work by Meibom et al. (2015), the rotation period of HAT-P-36 should correspond to an age of about 1.8 Gyr, which is close to the lower limit reported in Table 8, as derived from our isochrone-fitting analysis. Since the planet is very close to its host, we may speculate about tidal interactions affecting the evolution of the orbit and of the stellar spin. Assuming a modified tidal quality factor $Q'_* = 10^6$, the remaining lifetime of the system – i.e., the time left before the planet plunges into the star – is only 35 Myr (Metzger et al. 2012). Such rapid orbital decay should be accompanied by a negative transit time variation O-C of about 20 seconds in ten years that would be easy to measure with a space-borne photometer. On the other hand, if we assume $Q'_* \sim 10^7 - 10^8$, as suggested by Ogilvie & Lin (2007), the orbital decay and alignment timescales are a few hundred Myr or a few Gyr, respectively. They are shorter than or comparable to the estimated age of the star. In conclusion, in this scenario the present alignment could result from the tidal interaction during the main-sequence lifetime, while the remaining lifetime of the system is at least a few

hundred Myr. In any case, HAT-P-36 is an interesting system for studying the orbital and stellar spin evolution, as resulting from the tidal interaction and the magnetic wind braking of the star.

For WASP-11, the relatively large semi-major axis and the low mass of the planet imply, on the other hand, a weak tidal interaction with an angular momentum exchange timescale that is comparable to or longer than the age of the star. Therefore, the observed projected alignment of the system is likely to have a primordial origin.

Finally, for the HAT-P-36 system, we were able to also estimate its true obliquity, i.e. the angle, ψ, between the axes of the stellar rotation and the planetary orbit, obtaining an upper limit of $\psi < 63$ degrees. According to TEPCat, there are now 12 TEP systems for which we have the measurement of ψ. These values are plotted against the stellar temperature in Fig. 12, which does not highlight any particular correspondence between the two quantities.

The results presented in this work agree with the idea that stars with relatively cool photospheres should have small spin-orbit misalignment angles. However, looking at the entire sample of known TEP systems, for which we have an accurate estimation of λ, there are several exceptions to this scenario. In this context, the case of HAT-P-18 b (Esposito et al. 2014) is emblematic. The collection of more data is thus mandatory for disentangling the issue and understanding whether orbital obliquity really holds imprints of past migration processes that dramatically affected the evolution of giant planets.

References

Albrecht, S., Winn, J. N., Butler, R. P., et al. 2012a, ApJ, 744, 189
Albrecht, S., Winn, J. N., Johnson, J. A., et al. 2012b, ApJ, 757, 18
Anderson, D. R., Hellier, C., Gillon, M., et al. 2010, ApJ, 709, 159
Bakos, Á G., Pál, A., Torres, G., et al. 2009, ApJ, 696, 1950
Bakos, Á G., Hartman, J. D., Torres, G., et al. 2012, AJ, 144, 19
Baranne, A., Queloz, D., Mayor, M., et al. 1996, A&AS, 119, 373
Berdyugina, S. V. 2005, Liv. Rev. Sol. Phys., 2, 8
Biazzo, K., D'Orazi, V., Desidera, S., et al. 2012, MNRAS, 427, 2905
Brothwell, R. D., Watson, C. A., Hébrard, G., et al. 2014, MNRAS, 440, 3392
Casagrande, L., Ramírez, I., Meléndez, J., Bessell, M., & Asplund, M. 2010, A&A, 512, A54
Ciceri, S., Mancini, L., Southworth, J., et al. 2013, A&A, 557, A30
Claret, A. 2004, A&A, 424, 919
Cosentino, R., Lovis, C., Pepe, F., et al. 2012, in Proc. SPIE, 8446, 1V
Covino, E., Esposito, M., Barbieri, M., et al. 2013, A&A, 554, A28
Damasso, M., Biazzo, K., Bonomo, A. S., et al. 2015, A&A, 575, A111
Dawson, R. I. 2014, ApJ, 790, 31
Demarque, P., Woo, J.-H., Kim, Y.-C., & Yi, S. K. 2004, ApJS, 155, 667
Desidera, S., Sozzetti, A., Bonomo, A. S., et al. 2013, A&A, 554, A29
Desidera, S., Bonomo, A. S., Claudi, R. U., et al. 2014, A&A, 567, L6
Dotter, A., Chaboyer, B., Jevremovìc, D., et al. 2008, ApJS, 178, 89
Ehrenreich, D., & Désert, J.-M. 2011, A&A, 529, A136
Esposito, M., Covino, E., Mancini, L., et al. 2014, A&A, 564, L13
Hébrard, G., Ehrenreich, D., Bouchy, F., et al. 2011, A&A, 527, L11

Hilditch, R. W. 2001, An Introduction to Close Binary Stars (Cambridge, UK: Cambridge University Press)
Huitson, C. M., Sing, D. K., Pont, F., et al. 2013, MNRAS, 434, 3252
Knutson, H. A., Charbonneau, D., & Noyes, R. W. 2007, ApJ, 655, 564
Knutson, H. A., Howard, A. W., & Isaacson, H. 2010, ApJ, 720, 1569
Kovács, G., Bakos, G. Á., & Noyes, R. W. 2005, MNRAS, 356, 557
Kuschnig, R., Weiss, W. W., Gruber, R., Bely, P. Y., & Jenkner, H. 1997, A&A, 328, 544
Lendl, M., Triaud, A. H. M. J., Anderson, D. R., et al. 2014, A&A, 568, A81
Lund, M. N., Lundkvist, M., Silva Aguirre, V., et al. 2014, A&A, 570, A54
Maciejewski, G., Puchalski, D., Saral, G., et al. 2013, IBVS, 6082, 1
Mamajek, E. E., & Hillenbrand, L. A. 2008, ApJ, 687, 1264
Mancini, L., Southworth, J., Ciceri, S., et al. 2013a, A&A, 551, A11
Mancini, L., Ciceri, S., Chen, G., et al. 2013b, MNRAS, 436, 2
Mancini, L., Southworth, J., Ciceri, S., et al. 2014, MNRAS, 443, 2391
Mayor, M., & Queloz, D. 1995, Nature, 378, 355
Meibom, S., Barnes, S. A., Platais, I., et al. 2015, Nature, 517, 589
Metzger, B. D., Giannios, D., & Spiegel, D. S. 2012, MNRAS, 425, 2778
Mohler-Fischer, M., Mancini, L., Hartman, J., et al. 2013, A&A, 558, A55
Mordasini, C., Mollière, P., Dittkrist, K.-M., et al. 2015, Int. J. Astrobiol., 14, 201
Noyes, R. W., Hartmann, L. W., Baliunas, et al. 1984, ApJ, 279, 763
Ogilvie, G., & Lin, D. 2007, ApJ, 661, 1180
Pepe, F., Mayor, M., Galland, F., et al. 2002, A&A, 388, 632
Pietrinferni, A., Cassisi, S., Salaris, M., & Castelli, F. 2004, ApJ, 612, 168
Rabus, M., Alonso, R., Belmonte, J. A., et al. 2009, A&A, 494, 391
Sada, P. V., Deming, D., Jennings, D. E., et al. 2012, PASP, 124, 212
Sanchis-Ojeda, R., Winn, J. N., & Holman, M. J. 2011, ApJ, 733, 127
Sanchis-Ojeda, R., Winn, J. N., & Marcy, G. W. 2013, ApJ, 775, 54
Seager, S., & Mallén-Ornelas, G. 2003, ApJ, 585, 1038
Silva, A. V. R. 2003, ApJ, 585, L147
Silva-Valio, A., Lanza, A. F., Alonso, R., & Barge, P. 2010, A&A, 510, A25
Sing, D. K., Pont, F., Aigrain, S., et al. 2011, MNRAS, 416, 1443
Sneden, C. 1973, ApJ, 184, 839
Southworth, J. 2008, MNRAS, 386, 1644
Southworth, J. 2011, MNRAS, 417, 2166
Southworth, J. 2012, MNRAS, 426, 1291
Southworth, J. 2013, A&A, 557, 119
Southworth, J., Wheatley, P. J., & Sams, G. 2007, MNRAS, 379, L11
Southworth, J., Hinse, T. C., Burgdorf, M., et al. 2014, MNRAS, 444, 776
Sozzetti, A., Torres, G., Charbonneau, D., et al. 2007, ApJ, 664, 1190
Strassmeier, K. G. 2009, A&AR, 17, 251
Tregloan-Reed, J., Southworth, J., & Tappert, C. 2013, MNRAS, 428, 3671
Tregloan-Reed, J., Southworth, J., & Burgdorf, M. 2015, MNRAS, 450, 1760
Triaud, A. H. M. J., Collier Cameron, A., Queloz, D., et al. 2010, A&A, 524, A25
VandenBerg, D. A., Bergbusch, P. A., & Dowler, P. D. 2006, ApJS, 162, 375
Vaniĉek, P. 1971, Ap&SS, 12, 10
Wang, X., Gu, S., Collier Cameron, A., et al. 2014, AJ, 147, 92
West, R. G., Collier Cameron, A., Hebb, L., et al. 2009, A&A, 502, 395
Winn, J. N., Holman, M. J., Henry, G. W., et al. 2007, AJ, 133, 1828

Table 1. HARPS-N RV measurements of HAT-P-36 and WASP-11/HAT-P-10.

BJD(TDB)	RV (m s^{-1})	Error (m s^{-1})
HAT-P-36:		
2 456 345.583549	−16 200.7	5.5
2 456 345.594369	−16 213.9	5.8
2 456 345.605189	−16 227.2	4.6
2 456 345.616014	−16 249.9	4.6
2 456 345.626843	−16 240.2	5.5
2 456 345.637659	−16 247.8	5.3
2 456 345.648483	−16 266.6	7.4
2 456 345.659304	−16 306.0	5.5
2 456 345.670130	−16 352.7	6.4
WASP-11/HAT-P-10:		
2 456 933.502525	4907.4	8.0
2 456 933.509760	4901.6	6.5
2 456 933.516999	4907.8	4.5
2 456 933.524234	4902.7	3.8
2 456 933.531469	4905.5	3.7
2 456 933.538699	4910.1	3.5
2 456 933.545929	4902.3	4.1
2 456 933.553165	4907.2	3.5
2 456 933.560400	4908.2	4.0
2 456 933.567644	4902.8	3.5
2 456 933.574884	4913.1	3.3
2 456 933.582122	4913.4	3.9
2 456 933.589366	4907.7	3.7
2 456 933.596598	4903.3	4.2
2 456 933.603834	4904.6	4.0
2 456 933.611071	4899.7	4.2
2 456 933.618316	4891.2	4.2
2 456 933.625565	4887.1	3.3
2 456 933.632809	4880.9	3.5
2 456 933.640053	4879.5	3.5
2 456 933.647298	4877.8	3.2
2 456 933.654533	4877.9	3.8
2 456 933.661763	4879.4	3.7
2 456 933.669002	4885.9	3.7
2 456 933.676238	4887.0	3.8
2 456 933.683469	4891.0	4.1
2 456 933.690700	4884.7	3.7
2 456 933.697935	4881.6	3.8
2 456 933.705166	4884.5	3.5
2 456 933.712397	4873.5	4.0
2 456 933.719632	4881.2	4.3
2 456 933.726867	4879.8	4.2

Appendix A: Supplementary tables

The tables in this Appendix contain the detailed results of the predictions of different sets of stellar evolutionary models for the HAT-P-36 and WASP-11/HAT-P-10 planetary systems. The final values of the physical parameters for each of the two systems (see Tables 8 and 9), are calculated by taking the unweighted mean of the five estimates of the different sets of model predictions (see Sect. 5).

Table A.1. Derived physical properties of the HAT-P-36 system based on the prediction of different theoretical models.

	Claret models	Y^2 models	BaSTI models	VRSS models	DSEP models
K_b (km s^{-1})	196.19 ± 4.95	196.09 ± 1.79	193.00 ± 1.62	193.00 ± 2.76	196.17 ± 0.32
$M_\star$ ($M_\odot$)	1.0503 ± 0.0840	1.0486 ± 0.0287	1.0000 ± 0.0259	1.0000 ± 0.0426	1.0500 ± 0.0045
$R_\star$ ($R_\odot$)	1.048 ± 0.029	1.047 ± 0.012	1.031 ± 0.013	1.031 ± 0.018	1.048 ± 0.010
$\log g_\star$ (cgs)	4.4192 ± 0.0132	4.4190 ± 0.0100	4.4121 ± 0.0092	4.4121 ± 0.0109	4.4192 ± 0.0085
M_p (M_{Jup})	1.877 ± 0.130	1.875 ± 0.088	1.816 ± 0.087	1.816 ± 0.095	1.876 ± 0.079
R_p (R_{Jup})	1.313 ± 0.038	1.312 ± 0.020	1.291 ± 0.021	1.291 ± 0.025	1.313 ± 0.018
ρ_p (ρ_{Jup})	0.776 ± 0.049	0.776 ± 0.046	0.789 ± 0.047	0.789 ± 0.048	0.776 ± 0.047
Θ	0.0654 ± 0.0033	0.0654 ± 0.0030	0.0665 ± 0.0030	0.0665 ± 0.0032	0.0654 ± 0.0030
a (AU)	0.024040 ± 0.000605	0.024028 ± 0.000219	0.023651 ± 0.000198	0.023651 ± 0.000338	0.024038 ± 0.000036
Age (Gyr)	$4.3^{+2.4}_{-1.4}$	$4.0^{+1.1}_{-0.8}$	$7.6^{+4.3}_{-1.9}$	$5.0^{+1.5}_{-2.0}$	$1.7^{+7.5}_{-0.1}$

Notes. In each case $g_p = 27.0 \pm 1.4$ m s^{-2}, $\rho_\star = 0.913 \pm 0.027 \rho_\odot$ and $T_{eq} = 1788 \pm 15$ K.

Table A.2. Derived physical properties of the WASP-11/HAT-P-10 system based on the prediction of different theoretical models.

	Claret models	Y^2 models	BaSTI models	VRSS models	DSEP models
K_b (km s^{-1})	129.9 ± 3.2	127.7 ± 2.0	127.5 ± 1.9	127.5 ± 2.3	128.4 ± 2.1
$M_\star$ ($M_\odot$)	0.846 ± 0.063	0.804 ± 0.039	0.800 ± 0.036	0.800 ± 0.043	0.818 ± 0.038
$R_\star$ ($R_\odot$)	0.785 ± 0.023	0.772 ± 0.013	0.771 ± 0.015	0.771 ± 0.014	0.777 ± 0.012
$\log g_\star$ (cgs)	4.576 ± 0.016	4.569 ± 0.016	4.568 ± 0.015	4.568 ± 0.018	4.571 ± 0.018
M_p (M_{Jup})	0.508 ± 0.028	0.492 ± 0.020	0.490 ± 0.019	0.490 ± 0.024	0.497 ± 0.023
R_p (R_{Jup})	1.006 ± 0.031	0.989 ± 0.019	0.987 ± 0.020	0.987 ± 0.023	0.995 ± 0.022
ρ_p (ρ_{Jup})	0.467 ± 0.028	0.475 ± 0.025	0.476 ± 0.026	0.476 ± 0.027	0.472 ± 0.026
Θ	0.0531 ± 0.0021	0.0540 ± 0.0016	0.0541 ± 0.0017	0.0541 ± 0.0019	0.0537 ± 0.0019
a (AU)	0.04447 ± 0.00111	0.04373 ± 0.00069	0.04365 ± 0.00065	0.04365 ± 0.00080	0.04398 ± 0.00070
Age (Gyr)	$5.7^{+5.8}_{-4.8}$	$8.^{+3.9}_{-3.9}$	...	...	$6.2^{+2.7}_{-2.5}$

Notes. In each case $g_p = 12.45 \pm 0.50$ m s^{-2}, $\rho_\star = 1.748 \pm 0.074 \rho_\odot$ and $T_{eq} = 992 \pm 14$ K. We were not able to constrain a reasonable value for the age of the WASP-11/HAT-P-10 system by using the BaSTI and VRSS models, because the evolution of a star of the mass of WASP-11 is short for times shorter than the age of the Galaxy.